Applied Physics B (2022) 128:92
https://doi.org/10.1007/s00340-022-07812-z

Applied Physics B
Lasers and Optics

Dynamic three-wavelength imaging and volumetry of flowing cells with doubled field of view by six-pack holography

Simcha K. Mirsky[1] · **Natan T. Shaked**[1]

Received: 22 February 2022 / Accepted: 28 March 2022

Abstract
We present a new six-pack holography (6PH) system for simultaneous acquisition of six off-axis holograms in a single exposure from two fields of view and three wavelengths. The system is based on an external 6PH module, placed at the output of an inverted microscope, presenting a significantly more elegant solution compared to previous 6PH systems, which were based on cumbersome Mach–Zehnder interferometers built around the sample. This is also the first time in which six-pack holography is utilized for multi-wavelength imaging. We demonstrate using the new system to acquire volumetric data of flowing erythrocytes with twice the field of view of previous multi-wavelength holographic techniques. This volumetric data includes mean corpuscular volume, mean corpuscular hemoglobin (Hb) concentration, mean corpuscular Hb, and sphericity.

1 Introduction

Rapid imaging is one of the foundations of imaging flow cytometry, as the time required to complete many cytometric tests depends on how many cells may be imaged per second. This acquisition rate is typically limited by two parameters. First, the exposure time of the camera, which must be short enough to avoid motion blur, yet long enough to produce good image contrast. Second, the field of view (FOV) of the microscope system, which limits the number of cells that can be acquired in each exposure.

In this work, we present a new six-pack multiplexed off-axis holographic technique, whereby the FOV is doubled, in addition to the simultaneous acquisition of three different wavelength imaging channels. We then present the application of this technique to imaging flow cytometry and volumetry of erythrocytes (red blood cells, RBCs).

Until now, multiple techniques for extracting the volumetric data of cells from holograms have been developed. As holographic imaging enables acquisition of the sample quantitative phase in addition to the amplitude, holography provides access to information on the 3D shape parameters of the sample, as well as refractive index (RI) values, which are dependent on solute concentrations [1]. In the past, the quantitative phase maps produced by holography have been used in flow cytometry to extract morphological features and cellular drymass for the classification of various cells without labelling [2–8]. However, the sample thickness and RI are coupled, as per the following equation:

$$\Delta\phi(x,y,\lambda) = \frac{2\pi}{\lambda}\left[n_s(x,y,\lambda) - n_m(x,y,\lambda)\right]h(x,y), \tag{1}$$

where $\Delta\phi$ is the phase, n_s is the sample RI, n_m is the medium RI, and h is the sample thickness. This coupling makes determination of the sample index and height from phase maps non-trivial and requires additional data to separate these quantities, even for simple cells such as RBCs where one may assume n_s to be nearly uniform. One technique for decoupling is based on capturing two quantitative phase images of the sample while changing the medium [9–11]. Another technique uses a dispersive medium and two phase images of different wavelengths [12]. Additionally, tomographic phase microscopy can reconstruct the 3D RI map by acquiring quantitative phase images from multiple illumination angles or views of the sample [13, 14]. Finally, capturing three or more phase images of different wavelengths sequentially enables decoupling without altering the sample medium or scanning numerous angles [15].

These techniques, however, are not suitable for rapid imaging flow cytometry due to the need to alter the medium or scan the sample over time. Jang et al. [16] proposed an alternative technique for acquisition of RBC volumetric data using a single-shot spectroscopic holography technique.

✉ Natan T. Shaked
nshaked@tau.ac.il

[1] Department of Biomedical Engineering, Faculty of Engineering, Tel Aviv University, 69978 Tel Aviv, Israel

Published online: 18 April 2022

Three off-axis holograms of three different wavelengths are acquired simultaneously using a color camera to filter between the red, green, and blue light. Based on these multi-wavelength holograms, three equations are formulated for the three unknowns: hemoglobin (Hb) concentration, RBC height, and RI of non-Hb molecules. More recently, Turko et al. [17] proposed an optical system whereby this method may be applied by off-axis angular multiplexing of the three holograms on a grayscale camera, thus avoiding possible wavelength overlaps on the color camera pixels, as well as decreasing the effective pixel size in comparison to that of a color camera. In general, three-imaging-channel off-axis holographic multiplexing leaves unused space in the spatial frequency domain that may be used to acquire additional information. The optimal compression is defined by the six-pack holography (6PH) multiplexing theory [18].

6PH is an off-axis holographic angular multiplexing technique, whereby six holograms are acquired simultaneously in a single camera exposure. In standard off-axis holography, one sample beam that passes through the sample and one reference beam which contains no sample information interfere on the camera with a small angle between them to produce parallel off-axis fringes. These fringes act as a carrier frequency for the complex wave front data of the sample. In the spatial frequency domain, obtained by performing a 2D Fourier transform, this results in a single cross-correlation (CC) term and the corresponding complex conjugate term, as well as the autocorrelation (DC) terms, as illustrated in Fig. 1a. This single CC term may then be cropped and an inverse Fourier transform applied to reproduce the complex wave front image containing the quantitative phase profile of the sample. In 6PH, six different sample beams are interfered with six different reference beams on the camera at different and precise off-axis angles around the optical axis, simultaneously creating fringes of different orientations, resulting in six CC-term pairs in the corresponding spatial frequency domain, as illustrated in Fig. 1b. Each of the different six terms acquired in the single camera exposure may be cropped and used to reconstruct a different quantitative phase map, as there is no overlap between terms.

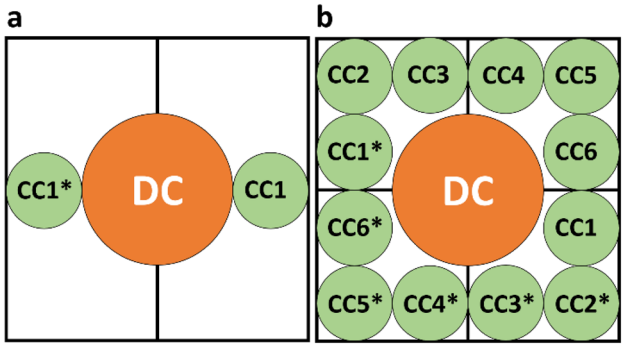

Fig. 1 Illustration of standard off-axis holography and 6PH spatial frequency domains. **a** Standard off-axis holography. **b** 6PH. CC1–CC6, CC terms, each of which encodes a different sample wave front; CC1*–CC6*, corresponding complex conjugate terms; DC, autocorrelation terms

In the past, we have demonstrated that this 6PH technique may be applied to dynamic synthetic aperture super resolution [19] and rejection of out-of-focus objects in amplitude images [20] for a single wavelength. However, these systems were based on large Mach–Zehnder interferometers built around an inverted microscope. In this work, we present a new and more elegant system for achieving 6PH and apply it to off-axis holographic imaging of two simultaneous FOVs of three different wavelengths. We demonstrate application of this system to dynamic volumetry of flowing RBCs with a doubled FOV. The proposed system represents the first external 6PH module, which may be placed at the output of an inverted microscope, as well as the first multi-wavelength six-pack system.

2 Methods

2.1 Holographic system

The three-wavelength six-pack holography system is an external module placed at the exit of an inverted microscope, as shown in Fig. 2. The microscope uses a three-wavelength coherent illumination source, TWL, comprised of a supercontinuum laser source (NKT SuperK EXTREME) coupled to an acousto-optical tunable filter (NKT SuperK SELECT). The TWL emits light of wavelengths 692, 532, and 490 nm, each with a full width at half maximum of approximately 6 nm, and corresponding coherence lengths of 35, 21, and 18 μm, respectively. More coherent light sources may be used as well. The multi-wavelength beam then passes though quarter waveplate QWP and is circularly polarized. The beam then illuminates the sample S, which is imaged by the inverted microscope comprised of microscope objective MO (Motic Plan Apo ELWD 20×, NA: 0.42) and tube lens TL (focal length 180 mm). All lenses in the system, including TL, are achromatic. The sample beam exits the inverted microscope and enters the external six-pack module, where it is split into the reference arm and sample arm by 50:50 beam splitter BS1.

In the sample arm, the beam passes through lens L1 (focal length 150 mm) and is split into two sample beams by 50:50 beam splitter BS2. One sample beam passes through polarizer P 0°, while the other sample beam passes through polarizer P 90°, which grants the two sample beams orthogonal polarizations, preventing them from interfering with each other. The sample beams are then reflected back through BS2 by mirrors M1 and M2 respectively, and a slight tilt in opposing directions to each mirror causes shearing in the

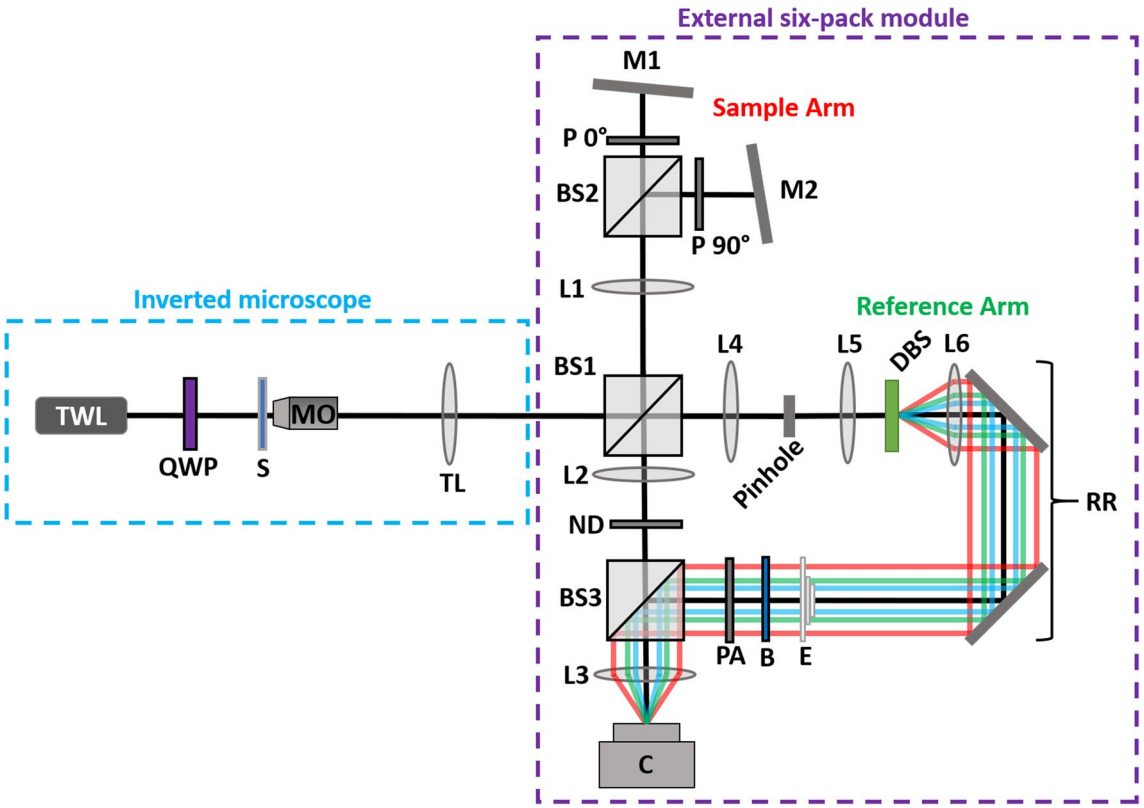

Fig. 2 Diagram of three-wavelength double FOV 6PH system. TWL, three-wavelength coherent light source; QWP, quarter waveplate; S, sample; MO, microscope objective lens; TL, tube lens; BS1–BS3, beam splitters; L1–L6, lenses; P 0°, polarizer with axis at 0°; P 90°, polarizer with axis at 90° relative to P 0°; M1–M2, mirrors; ND, neutral density filter; DBS, diffractive beam splitter; RR, retroreflector; E, echelon; B, beam stop; PA, polarizing array; C, camera. Black line indicates the optical axis, colored lines between DBS and C illustrate the reference beam paths per wavelength

image plane once the sample beams pass back through L1, resulting in the overlay of two different FOVs. The sample beams then pass back through BS1 and proceed through lenses L2 and L3 (with focal lengths 75 and 150 mm, respectively), which double the magnification, and neutral density filter ND (optical density 1) which matches the sample beam intensities to the reference beam intensities, while also passing through 50:50 beam splitter BS3 along the way. The two different FOVs are then projected onto camera C (FLIR GS3-U3-23S6M, 12-bit monochromatic CMOS, 1920 × 1200 square pixels of 5.86 µm each). The final magnification of the system is 37×, with a diffraction limited spot size of 1.65 µm.

In the reference arm, the image from the microscope is Fourier transformed by lens L4 (focal length 75 mm) and a 30 µm pinhole in the Fourier plane spatially filters the beam, removing the sample spatial information and creating a clean reference beam. This reference beam then passes through lens L5 (focal length 100 mm), thereby magnifying the beam by a factor of 1.33. The reference beam is then diffracted into a diverging 11 × 7 pattern of collimated beams by diffractive beam splitter DBS (DigitalOptics Corporation), which are then made to travel in parallel by lens L6 (focal length 150 mm). The reference beams then travel through retroreflector RR comprised of two mirrors mounted on a translation stage, such that RR may be moved left or right relative to the orientation shown in the figure. This enables the optical path of the reference arm to be matched to that of the sample arm. The reference beams then pass through custom-made glass echelon E, which equalizes the optical paths of the different wavelength beams. The reference beams then reach custom-made beam stop B, where only six reference beams are allowed to pass, two of each wavelength, as illustrated in Fig. 3. The reference beams are selected from the edges of the central 7 × 7 square pattern of beams, to provide the correct off-axis angles for 6PH. The six beams then pass through polarizing array PA, where the two groups of three reference beams of different wavelengths are orthogonally polarized relative to one another, such that for each wavelength, there are now two reference beams orthogonally polarized to each other, each matching one of the sample beam polarizations, thereby preventing unwanted interference between non-matching beam pairs. Finally, the reference beams combine with the sample beams in BS3

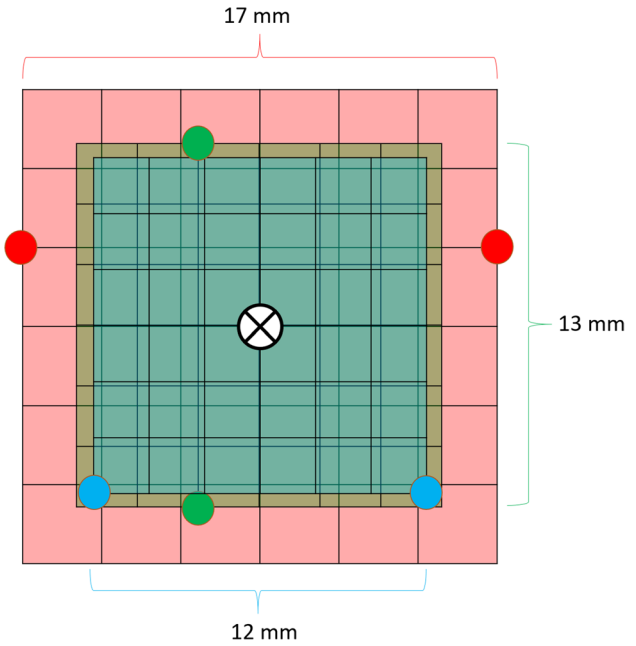

Fig. 3 Reference beam positions at echelon, shown in the direction of propagation. Red, green, and blue dots represent 692, 532, and 490 nm wavelength beams, respectively. Grid patterns show the approximate relative distances from the optical axis, marked ⊠. The pattern for each wavelength differs in size, with the width shown by the matching color braces

and are projected at the correct off-axis angles onto camera C by L3, producing the six-pack hologram. All lenses in the system are arranged in a 4f configuration, with M1 and M2 positioned one focal length from L1, the pinhole positioned at the shared focal point between L4 and L5, DBS positioned one focal length in front of L6, and B positioned one focal length from L6. The only exception is the distance between L5 and DBS, which is approximately 25.5 cm. This is necessary to match the sample and reference arm optical path lengths.

While the proposed system is relatively complex, the only significant challenge in alignment is in the beam stop, which must be carefully aligned such that the correct six beams shown in Fig. 3 are allowed to pass. A different set of wavelengths will require a different beam stop. Additionally, while the proposed system uses a 20× microscope objective lens, other microscope objective lenses may be used as well, though the ratio of diffraction limited spot size to total system magnification must be maintained to prevent CC terms from overlapping and to receive optimal FOV. This ratio is generally maintained when using objective lenses from the same manufacturer, as long as the immersion medium is unchanged (e.g. only lenses operating in air and not oil). Lastly, when altering magnification, it may be necessary to slightly adjust the angles of M1 and M2 to achieve optimal doubled FOV.

2.2 Quantitative phase reconstruction process

Video six-pack holograms of the sample were recorded at 19 frames per second, with an exposure time of 52.51 ms. Each frame was then digitally 2D Fourier transformed and the six CC terms were cropped, zero padded, and inverse 2D Fourier transformed to produce six complex wave front images. These images were then numerically refocused by at most 14 μm using Fresnel propagation [21] to compensate for chromatic aberrations caused by the cubic beam splitters. The same process was applied to a background image containing no sample, and all sample complex wave front images were pixel-wise divided by the background complex wave front to compensate for phase curvature. Next, a windowed Fourier transform filter [22, 23] was applied to reduce image noise. Finally, the phase was extracted from the exponents of these images, and unwrapping was performed using Miguel's 2D unwrapping algorithm [24], producing six unwrapped quantitative phase images.

2.3 Volumetric RBC cytometry measurements

For RBCs, the phase delay, $\Delta\phi$, can be expressed as a function of wavelength λ, a constant β [25, 26], Hb concentration C, the average RI of non-Hb molecules in the RBC relative to the RI of the medium n_x, and cell height h, as per the following equation [16]:

$$\Delta\phi(x, y, \lambda) = \frac{2\pi}{\lambda}\left[\beta(\lambda)C(x, y) + n_x(x, y)\right]h(x, y) \tag{2}$$

When using three wavelengths, this results in a system of three equations with three unknowns: C, n_x, and h. However, as the unknown variables are connected by multiplication, it is necessary to use an optimization algorithm to solve this problem [16]. In our case, we implemented the Matlab interior-point nonlinear optimization algorithm for finding the minimum of constrained nonlinear multivariable functions (Mathworks Inc.). For the optimization process, we used the following constraints to minimize the standard deviation (std) of C and n_x.

$$\min\left[\mathrm{std}\left(C, n_x\right)\right] = \begin{cases} 0.001 < n_x < 0.01 \\ 20 < C < 50\left[\frac{\mathrm{g}}{\mathrm{dl}}\right] \\ 0.1 < h < 3[\mu\mathrm{m}] \end{cases}. \tag{3}$$

Once the missing three variables were solved, we integrated h to find the cellular volume and determine the cell surface area (SA) by generating a 3D mesh surface from the 2D h map values and calculating its area, SA_{surf}. The surface area is then calculated based on the following equation by Mir et al. [27]

$$SA = 2 \cdot SA_{\text{surf}} + P \cdot h_{\text{min}}, \tag{4}$$

where P is the perimeter of the cell and h_{min} is the minimum optical path delay within the cell region. Following this, we calculated the sphericity index of the cell as follows [28]

$$\text{Sphericity} = 4.84\frac{V^{\frac{2}{3}}}{SA}. \tag{5}$$

where V is the cellular volume, or mean corpuscular volume (MCV). Sphericity is an important metric for RBCs, as it strongly correlates to the ability of the cell to fit through narrow capillaries. Lastly, mean corpuscular Hb concentration (MCHC) was calculated by taking the average of C, and the total mass of Hb present, also known as the mean corpuscular Hb (MCH) was derived by integrating C over the whole volume.

3 Results

To demonstrate the ability of the system to extract volumetric measurements from flowing RBCs in two FOV simultaneously, human blood was obtained from the Israeli blood bank, after obtaining Tel Aviv University's ethical approvals. The blood was diluted in phosphate buffered saline (PBS) containing ethylenediamine tetraacetic acid (EDTA) at a concentration of 2 mM to prevent coagulation. The sample suspension was then flowed through a microfluidic channel 1 mm wide and 100 μm tall (Ibidi, μ-Slide VI 0.1) at a speed of 14.1 μm/s using a syringe pump (New Era Pump Systems, NE-300). The six-pack hologram from a single video frame is shown in Fig. 4a, and the corresponding spatial frequency power spectrum produced by a digital 2D Fourier transform is shown in Fig. 4b, where it can be seen that there are indeed six CC terms and their complex conjugates, and there is no overlapping of the terms. An additional four faint terms caused by light scattered from the DBS are visible along the vertical and horizontal axes, however these terms are not included in the cropped CC terms used for reconstruction. The resulting three quantitative phase map images from the two overlapping FOVs are shown in Fig. 5a–c, and a quantitative phase map video of the flowing cells is shown in Visualization 1. In this visualization, we can see the dynamic six-pack hologram on the left, the reconstructed and combined doubled-FOV quantitative phase maps for each wavelength in the middle, and magnified sections of both FOVs where two different RBCs flow through in focus, simultaneously. The dashed white lines in this visualization and in Fig. 5a–c indicate the small region of overlap between the FOVs. While in this experiment we demonstrated slightly overlapping FOVs to better demonstrate their relative positions, the FOVs need not overlap at all. Magnified quantitative phase images of two cells, each from a different FOV, are show in Fig. 5d.

The volumetric parameters of each cell in these images were calculated as detailed above, resulting in MCV of 86.7 and 82.3 fl, MCHC of 34.4 and 34.6 g/dl, MCH of 29.8 and 28.6 pg, and sphericity indices of 0.74 and 0.85, respectively. These MCV, MCHC, and MCH values correspond to their respective established normal values of 80–94 fl, 32–36 g/dl, and 27–31 pg [29].

Angular multiplexing of holograms is expected to increase phase noise due to sharing the camera grayscale dynamic range. To assess the effect of noise in this system on the volumetric values in both FOVs, we tracked the cells from Fig. 5d across ten frames and acquired their volumetric values for each frame. The mean values and their standard deviations over these ten frames are shown in Fig. 6. The average value of the standard deviations of all metrics as a percent of their respective mean values was 3% for the cell from FOV #1 and 2% for the cell from FOV #2, indicating

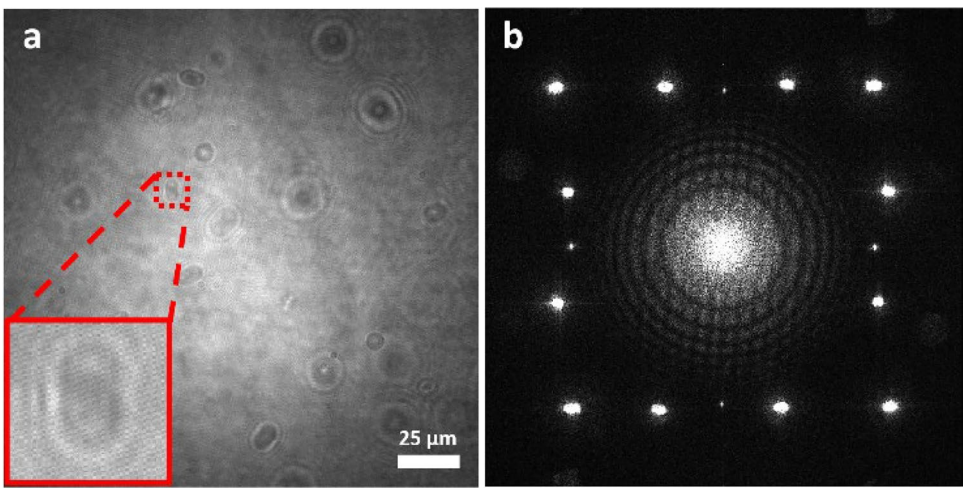

Fig. 4 Six-pack hologram and resulting spatial frequency power spectrum. **a** Six-pack multiplexed hologram. Inlay is magnified ×5 to show the multiplexed interference fringes. **b** Spatial frequency power spectrum of **a**

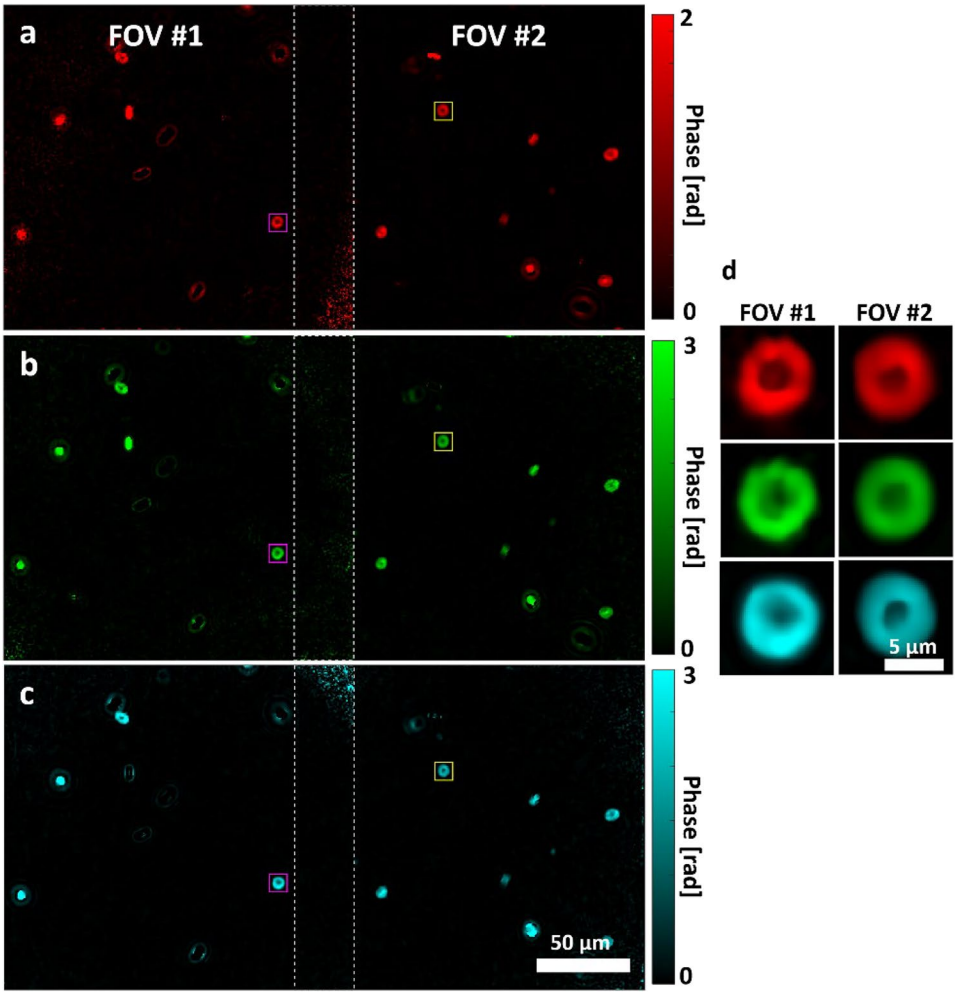

Fig. 5 Quantitative phase maps of combined doubled FOVs. **a** Combined phase map of both FOVs for 692 nm wavelength. **b** Combined phase map of both FOVs for 532 nm wavelength. **c** Combined phase map of both FOVs for 490 nm wavelength. Scale bar in (**c**) also applies to (**a**, **b**). **d** Enlarged RBC phase maps from (**a**–**c**). FOV #1 phase maps are of a cell flowing inside the small magenta square on the left of (**a**–**c**), FOV #2 phase maps are of a cell flowing inside the small yellow square on the right of (**a**–**c**). Scale bar applies to all phase maps in (**d**)

that the system noise had a minimal effect on the volumetric measurements.

4 Conclusion

We have demonstrated the first external 6PH system and the first multi-wavelength 6PH system, and have shown that this system may be applied to double the FOV for volumetric measurement of RBCs flowing in a microchannel, effectively doubling the rate at which these spectroscopic measurements may be performed on a sample. In addition, the effect of the multiplexing noise on the measurements was tested and shown to be minimal. Furthermore, as there is no overlap between the CC terms in 6PH, the technique is not limited to sparse samples, thus it may also image a densely flowing monolayer of cells.

In the future, the system may be further optimized using a DBS that generates only twelve beams in a square pattern, thereby enabling a potential seven-fold increase in reference beam intensity. Additionally, the reflection to transmission ratios of beam splitters BS1 and BS3 may be adjusted to be more conservative of sample beam intensity. Finally, it may be possible to replace the reference arm loop using a reflective DBS, thereby creating a setup more similar to a τ interferometer [30], though this would require specialized multifocal lenses.

As the channel used in this work was 100 µm tall, many cells were out of focus and cells may occasionally overlap. Regarding cell focus, out-of-focus cells may be numerically refocused using Fresnel propagation, as was used to correct for chromatic aberrations. However, in the future, it would be possible to resolve both issues by optimizing the microchannel. A microchannel with a height of roughly 20 µm could be used to maintain cells near focus at all times, while preventing overlap, thereby enabling optimal acquisition of cell parameters across the entire doubled FOV at all times.

One of the many techniques utilizing the acquisition of multiple holograms of different wavelengths is the reduction of phase noise by averaging the different wavelength phase images [31, 32]. In the future, the proposed system may be able to implement this technique dynamically.

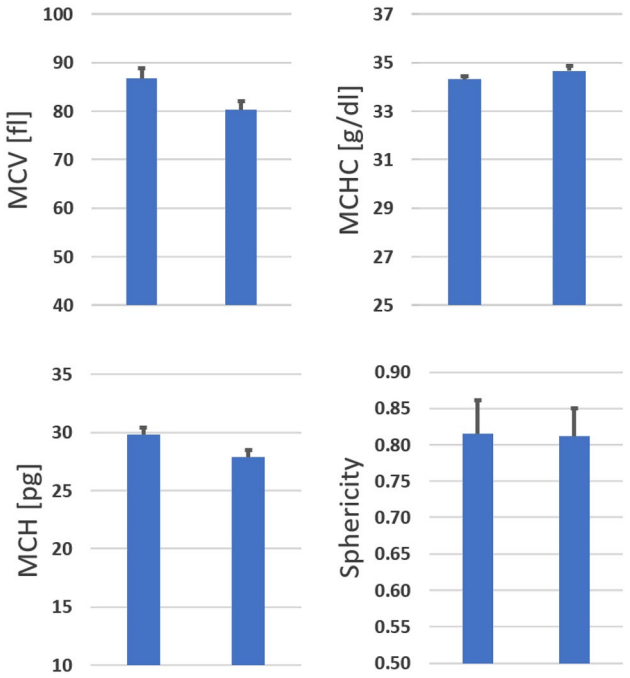

Fig. 6 Mean values for two cells, one from each FOV, over 10 frames, with indicated standard deviation to assess the effect of noise on the measurement stability. Left bars are of cell from FOV #1, right bars of cell from FOV #2. Mean MCV: 86.8 and 80.3 fl, std: 2.1 and 1.8 fl. Mean MCHC: 34.3 and 34.7, std: 0.1 and 0.2. Mean MCH: 29.8 and 27.9, std: 0.6 and 0.6. Mean sphericity: 0.82 and 0.81, std: 0.05 and 0.04

Other multi-wavelength holographic techniques, such as synthetic wavelength holography [33], may also be enhanced using the proposed system.

Supplementary Information The online version contains supplementary material available at https://doi.org/10.1007/s00340-022-07812-z.

Declarations

Conflict of interest The authors declare that they have no conflict of interest.

References

1. G. Popescu, *Quantitative Phase Imaging of Cells and Tissues* (McGraw-Hill Professional, New York, 2011)
2. D. Roitshtain, L. Wolbromsky, E. Bal, H. Greenspan, L. Satterwhite, N.T. Shaked, Cytometry A **91**, 5 (2017)
3. S.K. Mirsky, I. Barnea, M. Levi, H. Greenspan, N.T. Shaked, Cytometry A **91**, 9 (2017)
4. M. Ugele, M. Weniger, M. Stanzel, M. Bassler, S.W. Krause, O. Friedrich, O. Hayden, L. Richter, Adv. Sci. **5**, 12 (2018)
5. M. Ugele, M. Weniger, M. Leidenberger, Y. Huang, M. Bassler, O. Friedrich, B. Kappes, O. Hayden, L. Richter, Lab Chip **18**, 12 (2018)
6. J. Min, B. Yao, V. Trendafilova, S. Ketelhut, L. Kastl, B. Greve, B. Kemper, J. Biophotonics **12**, 9 (2019)
7. N. Nissim, M. Dudaie, I. Barnea, N.T. Shaked, Cytometry A **99**, 5 (2021)
8. L. Xin, W. Xiao, L. Che, J. Liu, L. Miccio, V. Bianco, P. Memmolo, P. Ferraro, X. Li, F. Pan, ACS Omega **6**, 46 (2021)
9. A.I. Yusipovich, EYu. Parshina, NYu. Brysgalova, A.R. Brazhe, N.A. Brazhe, A.G. Lomakin, G.G. Levin, G.V. Maksimov, J. Appl. Phys. **105**, 10 (2009)
10. B. Rappaz, A. Barbul, Y. Emery, R. Korenstein, C. Depeursinge, P.J. Magistretti, P. Marquet, Cytometry A **73**, 10 (2008)
11. B. Rappaz, F. Charrière, C. Depeursinge, P.J. Magistretti, P. Marquet, Opt. Lett. **33**, 7 (2008)
12. C. Yang, A. Wax, I. Georgakoudi, E.B. Hanlon, K. Badizadegan, R.R. Dasari, M.S. Feld, Opt. Lett. **25**, 20 (2000)
13. Y. Park, M. Diez-Silva, G. Popescu, G. Lykotrafitis, W. Choi, M.S. Feld, S. Suresh, Proc. Natl. Acad. Sci. USA **105**, 37 (2008)
14. M. Habaza, M. Kirschbaum, C. Guernth-Marschner, G. Dardikman, I. Barnea, R. Korenstein, C. Duschl, N.T. Shaked, Adv. Sci. **4**, 2 (2017)
15. Y. Park, T. Yamauchi, W. Choi, R. Dasari, M.S. Feld, Opt. Lett. **34**, 23 (2009)
16. Y. Jang, J. Jang, Y. Park, Opt. Express **20**, 9 (2012)
17. N.A. Turko, N.T. Shaked, Biomed. Opt. Express **11**, 11 (2020)
18. M. Rubin, G. Dardikman, S.K. Mirsky, N.A. Turko, N.T. Shaked, Opt. Lett. **42**, 22 (2017)
19. S.K. Mirsky, N.T. Shaked, Opt. Express **27**, 19 (2019)
20. S.K. Mirsky, N.T. Shaked, Opt. Express **29**, 2 (2021)
21. F. Dubois, L. Joannes, J. Legros, Appl. Opt. **38**, 34 (1999)
22. S. Montresor, P. Picart, Opt. Express **24**, 13 (2016)
23. Q. Kemao, Appl. Opt. **43**, 13 (2004)
24. M.A. Herráez, D.R. Burton, M.J. Lalor, M.A. Gdeisat, Appl. Opt. **41**, 35 (2002)
25. O. Zhernovaya, O. Sydoruk, V. Tuchin, A. Douplik, Phys. Med. Biol. **56**, 13 (2011)
26. M. Friebel, M. Meinke, Appl. Opt. **45**, 12 (2006)
27. M. Mir, Z. Wang, K. Tangella, G. Popescu, Opt. Express **17**, 4 (2009)
28. P.B. Canham, A.C. Burton, Circ. Res. **22**, 3 (1968)
29. H.K. Walker, W.D. Hall, J.W. Hurst, *Clinical Methods: The History, Physical, and Laboratory Examinations* (Butterworths, Boston, 1990)
30. N.T. Shaked: modul, 11 (2012)
31. B. Kemper, L. Kastl, J. Schnekenburger, S. Ketelhut, Proc. SPIE **10503**, 1050313 (2018)
32. C. Larivière-Loiselle, E. Bélanger, P. Marquet, Neurophoton. **7**, 4 (2020)
33. N.A. Turko, P.J. Eravuchira, I. Barnea, N.T. Shaked, Opt. Lett. **43**, 9 (2018)